A&A 671, A82 (2023)
https://doi.org/10.1051/0004-6361/202245192
© The Authors 2023

Astronomy & Astrophysics

Disk Evolution Study Through Imaging of Nearby Young Stars (DESTINYS): Characterization of the young star T CrA and its circumstellar environment⋆,⋆⋆

E. Rigliaco[1], R. Gratton[1], S. Ceppi[2], C. Ginski[3,4], M. Hogerheijde[3,4], M. Benisty[5,6], T. Birnstiel[7,8], M. Dima[1], S. Facchini[2], A. Garufi[9], J. Bae[10], M. Langlois[11], G. Lodato[2], E. Mamajek[12], C. F. Manara[13], F. Ménard[6], Á. Ribas[14], and A. Zurlo[15,16,17]

[1] INAF/Osservatorio Astronomico di Padova, Vicolo dell'osservatorio 5, 35122 Padova. Italy
e-mail: elisabetta.rigliaco@inaf.it
[2] Dipartimento di Fisica, Università Degli Studi di Milano, Via Celoria, 16, Milano 20133, Italy
[3] Anton Pannekoek Institute for Astronomy, University of Amsterdam, Science Park 904, 1098XH Amsterdam, The Netherlands
[4] Leiden Observatory, Leiden University, PO Box 9513, 2300 RA, Leiden, The Netherlands
[5] Unidad Mixta Internacional Franco-Chilena de Astronomía, CNRS/INSU UMI 3386, Departamento de Astronomía, Universidad de Chile, Camino El Observatorio 1515, Las Condes, Santiago, Chile
[6] Univ. Grenoble Alpes, CNRS, IPAG, 38000 Grenoble, France
[7] University Observatory, Faculty of Physics, Ludwig-Maximilians-Universität München, Scheinerstr. 1, 81679 Munich, Germany
[8] Exzellenzcluster ORIGINS, Boltzmannstr. 2, 85748 Garching, Germany
[9] INAF, Osservatorio Astrofisico di Arcetri, Largo Enrico Fermi 5, 50125 Firenze, Italy
[10] Department of Astronomy, University of Florida, Gainesville, FL 32611, USA
[11] CRAL, UMR 5574, CNRS, Université Lyon 1, 9 avenue Charles André, 69561 Saint-Genis-Laval Cedex, France
[12] Jet Propulsion Laboratory, California Institute of Technology, 4800 Oak Grove Drive, Pasadena, CA 91109, USA
[13] European Southern Observatory, Karl-Schwarzschild-Strasse 2, 85748 Garching bei München, Germany
[14] Institute of Astronomy, University of Cambridge, Madingley Road, Cambridge, CB3 0HA, UK
[15] Núcleo de Astronomía, Facultad de Ingeniería y Ciencias, Universidad Diego Portales, Av. Ejercito 441, Santiago, Chile
[16] Escuela de Ingeniería Industrial, Facultad de Ingeniería y Ciencias, Universidad Diego Portales, Av. Ejercito 441, Santiago, Chile
[17] Aix Marseille Univ, CNRS, CNES, LAM, Marseille, France

Received 12 October 2022 / Accepted 22 December 2022

ABSTRACT

Context. In recent years, a new hot topic has emerged in the star and planet formation field, namely, the interaction between the circumstellar disk and its birth cloud. The birth environments of young stars leave strong imprints on the star itself and their surroundings. In this context, we present a detailed analysis of the rich circumstellar environment around the young Herbig Ae/Be star T CrA.
Aims. Our aim is to understand the nature of the stellar system and the extended circumstellar structures, as seen in scattered light images.
Methods. We conducted our analysis on the basis of a set of combined archival data and new adaptive optics images at a high contrast and high resolution.
Results. The scattered light images reveal the presence of a complex environment around T CrA, composed of a bright, forward-scattering rim of the disk's surface that is seen at very high inclinations, along with a dark lane of the disk midplane, bipolar outflows, and streamer features that are likely tracing infalling material from the surrounding birth cloud onto the disk. The analysis of the light curve suggests that the star is a binary with a period of 29.6 yr, confirming previous assertions based on spectro-astrometry. The comparison of the scattered light images with the ALMA continuum and ^{12}CO (2–1) line emission shows that the disk is in Keplerian rotation and the northern side of the outflowing material is receding, while the southern side is approaching the observer. The overall system lies on different geometrical planes. The orbit of the binary star is perpendicular to the outflows and is seen edge on. The disk is itself seen edge-on, with a position angle of ∼7°. The direction of the outflows seen in scattered light is in agreement with the direction of the more distant molecular hydrogen emission-line objects (MHOs) associated with the star. Modeling of the spectral energy distribution using a radiative transfer scheme is in good agreement with the proposed configuration, as well as the hydrodynamical simulation performed using a smoothed particle hydrodynamics code.
Conclusions. We find evidence of streamers of accreting material around T CrA. These streamers connect the filament, along which T CrA is forming along with the outer parts of the disk, suggesting that the strong misalignment between the inner and outer disk is due to a change in the direction of the angular momentum of the material accreting on the disk during the late phase of star formation. This impacts the accretion taking place in the components of the binary, favoring the growth of the primary with respect the secondary, in contrast to the case of aligned disks.

Key words. circumstellar matter – stars: pre-main sequence – protoplanetary disks – ISM: individual objects: TCrA – ISM: jets and outflows

⋆ Reduced images are also available at the CDS via anonymous ftp to cdsarc.cds.unistra.fr (130.79.128.5) or via https://cdsarc.cds.unistra.fr/viz-bin/cat/J/A+A/671/A82

⋆⋆ Based on observations collected at the European Organisation for Astronomical Research in the Southern Hemisphere under ESO programme 1104.C-0415(H).

Open Access article, published by EDP Sciences, under the terms of the Creative Commons Attribution License (https://creativecommons.org/licenses/by/4.0), which permits unrestricted use, distribution, and reproduction in any medium, provided the original work is properly cited.
This article is published in open access under the Subscribe to Open model. Subscribe to A&A to support open access publication.

1. Introduction

Herbig Ae/Be stars (Herbig 1960) are pre-main sequence stars with intermediate mass that cover the range between low-mass T Tauri stars (TTSs) and embedded massive young stellar objects. The formation of stars in the low- and intermediate-mass regimes involves accreting disks that were formed during the collapse of the protostar, as well as fast collimated outflows and jets. The circumstellar environment of these objects is highly dynamic and multi-wavelength observations have shown a broad photometric and spectroscopic variability (e.g., Pikhartova et al. 2021; Mendigutía et al. 2011) that can be used as a tool for understanding the physics of accretion and ejection related to the interaction between the star and its circumstellar environment.

T CrA (RA = 19:01:58.79 Dec = −36:57:50.33) is an Herbig Ae/Be star member of the Coronet Cluster, belonging to the Corona Australis star-forming region, which is one of the nearest (149.4±0.4 pc, Galli et al. 2020) and most active regions of ongoing star formation. The Coronet Cluster is centered on the Herbig Ae/Be stars R CrA and T CrA. It is very active in terms of star formation (e.g., Lindberg & Jørgensen 2012), harboring many Herbig-Haro (HHs) objects and molecular hydrogen emission-line Objects (MHOs). It has been target of many surveys and all studies are in agreement with respect to an age assignation for Coronet of <3 Myr (e.g. Meyer & Wilking 2009; Sicilia-Aguilar et al. 2011). In this paper, we investigate the variable star T CrA, which was classified as F0 by Joy (1945), with an effective temperature $T_{\rm eff}$ = 7200 K – according to Cazzoletti et al. (2019) and Herczeg & Hillenbrand (2014), this corresponds to L_* ∼29 $L_\odot$ and a stellar mass of ∼2.25 $M_\odot$, using the evolutionary tracks by Siess et al. (2000) and adopting the average distance of 154 pc calculated by Dzib et al. (2018). The *Gaia*-DR2 and DR3 catalogs (Gaia Collaboration 2016, 2021) do not provide proper motion or parallax values for T CrA. This star was not observed by the Hipparcos satellite and it is also not listed in the UCAC5 catalog. The former UCAC4 catalog (Zacharias et al. 2012) provides a proper motion result ($\mu_\alpha \cos\delta$ = 2.0 ± 3.8 mas yr^{-1}, μ_δ = −22.6 ± 3.8 mas yr^{-1}) that is consistent with membership in Corona-Australis (within the large uncertainties of that solution). Galli et al. (2020) provided an updated census of the stellar population in the Corona Australis, deriving an average distance of 149.4 ± 0.4 pc. This is the distance we use throughout the paper. A deep H_2 v = 1–0 S(1) 2.12 μm narrow-band imaging survey of the northern part of the Corona Australis cloud conducted by Kumar et al. (2011) has identified many new MHOs (Davis et al. 2010). Among these objects, two are considered unambiguously associated to T CrA: MHO2013 and MHO2015; as seen in Fig. 3 in Kumar et al. (2011). MHO 2015 is a clear bow-shock feature, lying to the south of T CrA, and it marks the southern lobe of the bipolar outflow originating from T CrA. MHO 2013 marks the northern lobe. The hypothetical line connecting the two MHOs crosses the position of T CrA. This is the only unambiguously detected bipolar outflow traced by two complementing bow-shock features in the entire Coronet region (Kumar et al. 2011). We reproduce the image shown in Kumar et al. (2011) in the left panel of Fig. 1.

T CrA was suggested to be a binary system by Bailey (1998) and Takami et al. (2003). Using spectro-astrometry in the Hα line, they suggested that the system is a binary with a companion at >0.14″. However, no companion has been detected using spectro-astrometry in the fundamental rovibrational band of CO at 4.6 μm (Pontoppidan et al. 2011) nor with K-band speckle imaging (Ghez et al. 1997; Köhler et al. 2008). In the same years, infrared speckle observations performed by Ghez et al. (1997) did not show the presence of a stellar companion. The non-detection of the companion by Ghez et al. (1997) implies that the possible companion has a contrast in the K-band larger than 3 mag (that is a K-magnitude fainter than 10.5) or a separation smaller than 0.1 arcsec at the epoch of the observation (April 26, 1994; see also Takami et al. 2003).

The circumstellar environment of T CrA was recently investigated. The Faint Object infraRed CAmera for the SOFIA Telescope (SOFIA/FORCAST, Herter et al. 2018) observations show very strong excess in the far-infrared (FIR). T CrA was also detected in all *Herschel*/PACS (Photodetector Array Camera and Spectrometer) bands (Sandell et al. 2021), highlighting the presence of warm or hot dust. Mid-infrared interferometric data obtained with VLT/MID-infrared Interferometric instrument (VLT/MIDI) show the presence of disk emission from the inner regions, where the temperature is sufficiently high (Varga et al. 2018). The presence of the inner disk is also given by the spectral energy distribution (SED) which shows near-IR (NIR) excess emission (Sicilia-Aguilar et al. 2013). Optical and IR spectra covering the [OI] λ6300 and [NeII] 12.81 μm lines (Pascucci et al. 2020) show emission attributed to a jet nearly in the plane of the sky. Moreover, continuum ALMA observations of T CrA at 1.3 mm (230 GHz) were conducted as part of the survey of protoplanetary disks in Corona Australis (Cazzoletti et al. 2019) and the data show a ∼22σ detection at 1.34″ from the nominal Spitzer position that is considered to be a detection. The 1.3 mm continuum flux is then converted into a dust mass ($M_{\rm dust}$) under the assumption of optically thin and isothermal sub-millimeter emission, yielding $M_{\rm dust}$ = 3.64±0.27 $M_\oplus$. No information on the ^{12}CO(2–1) gas content in the disk has been provided. The average disk mass in CrA is 6 ± 3 $M_\oplus$, which is significantly lower than that of disks in other young (1–3 Myr) star-forming regions (Lupus, Taurus, Chamaeleon I, and Ophiuchus) and appears to be consistent with the average disk mass of the 5–10 Myr-old Upper Sco (Cazzoletti et al. 2019).

In this paper, we analyze images of T CrA acquired with the Very Large Telescope at ESO's Paranal Observatory in Chile. We employ polarimetric differential imaging (PDI) observations obtained with Spectro-Polarimetric High-contrast Exoplanet REsearch (SPHERE Beuzit et al. 2019) in the H band to explore the circumstellar environment by tracing light scattered by the small (μm-sized) dust grains. Moreover, we use archival photometric and imaging data to investigate the multiplicity of the system. The paper is organized as follows. In Sect. 2, we describe the data collected from the archive and newly acquired. In Sect. 3, we describe the data analysis. First, we discuss the multiplicity of the system as suggested by the photometric data, the analysis of the proper motion, and the analysis of the PSF subtracted images. Second, we analyze the geometry of the system with the analysis of the disk and the extended emission seen in scattered light. In Sect. 4, we propose a scenario that reconciles all the findings, showing a model of the system and discussing a modeling of the spectral energy distribution and hydrodynamical simulation. In Sect. 5, we present our summary and conclusions.

2. Observations

2.1. SPHERE data

T CrA was observed on 2021 June 6 with SPHERE/InfraRed Dual-band Imager and Spectrograph (IRDIS; Dohlen et al. 2008) in the dual-beam polarimetric imaging mode (DPI; de Boer et al. 2020; van Holstein et al. 2020) in the broadband H filter

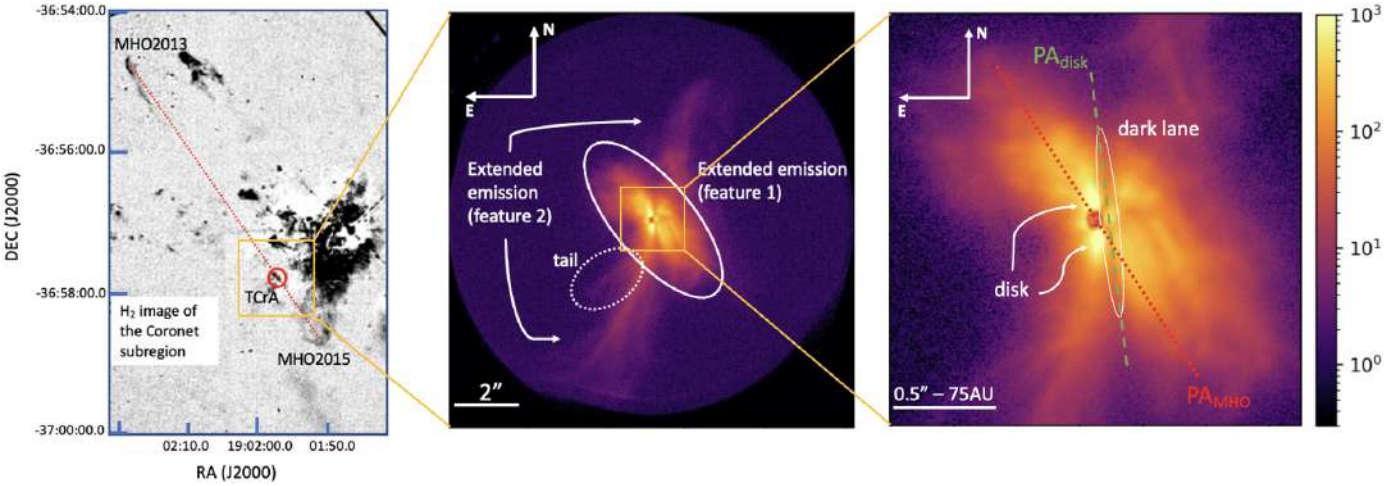

Fig. 1. SPHERE/IRDIS polarized light image in *H*-band of T CrA. Left panel: H_2 image of the Coronet sub-region. The image is adapted from Kumar et al. 2011. The red line shows the line connecting the two MHOs associated to T CrA. The orange box shows the IRDIS field of view. Middle panel: Field of view (∼12.5″) of the SPHERE/IRDIS polarized light image in *H*-band of T CrA. The extended emission features analyzed in the manuscript are labeled. The orange box shows the innermost region of the system. Right panel: Zoom-in on the innermost 2″ around the central system. The disk and the shielded disk mid-plane seen as dark lane are labeled.

with pupil tracking setting, as part of the Disk Evolution Study Through Imaging of Nearby Young Stars (DESTINYS, Ginski et al. 2020, 2021) program. An apodized Lyot coronagraph with an inner working angle of 92.5 mas was used to mask the central star. The individual frame exposure time was set to 32 s and a total of 136 frames were taken separately in 34 polarimetric cycles of the half-wave plate. The total integration time was 72.5 minutes. Observing conditions were excellent with an average seeing of 0.8″ and an atmosphere coherence time of 6.4 ms. In addition to the science images, flux calibration images were obtained by offsetting the star position by about 0.5 arcsec with respect to the coronagraph using the SPHERE tip/tilt mirror and inserting a suitable neutral density filter to avoid image saturation. Two flux calibration sequences were acquired – before and after the science observation. We used the IRDIS Data reduction for Accurate Polarimetry (IRDAP, van Holstein et al. 2020) public pipeline to reduce the data. The images were astrometrically calibrated using the pixel scale and true north offset given in Maire et al. (2016). Because the data were taken in pupil-tracking mode, we were able to perform an angular differential imaging (ADI; Marois et al. 2006) reduction in addition to the polarimetric reduction, resulting in a total intensity image and a polarized intensity image. We show the initial combined and flux calibrated Stokes Q and U images as well as the Q_Φ and U_Φ images in Appendix A.

Additional SPHERE observations of T CrA were acquired in 2016 and 2018 with the ESO programs 097.C-0591(A) and 0101.C-0686(A) (PI: Schmidt) in classical imaging mode, using a classical Lyot coronagraph and the broadband *H* filter (BB_H). The data were reduced through the SPHERE Data Center (Delorme et al. 2017). The 2016 data have very low S/N ratio and they are not usable for this work. The 2018 IRDIS data are instead of good quality and are used to confirm the features detected in the 2021 images.

2.2. NACO data

To perform our analysis, we also made use of archival NACO data. Adaptive optics corrected near-infrared imaging of T CrA was obtained with NAOS-CONICA (NACO; Lenzen et al. 2003; Rousset et al. 2003) at the VLT in July 12, 2007 (program ID 079.C-0103(A)), March 29, 2016 (program ID 097.C-0085(A)), and May 21, 2017 (program ID 099.C-0563(A)). In all cases, the images were obtained in *Ks* band ($\lambda_c = 2.18$ μm) using the S13 camera, with a 13.72 mas pixel^{-1} scale. In 2007, 3000 frames of 0.6 seconds were taken with an average seeing of 0.8. In 2016, 540 frames of 0.5 s each were taken with average seeing of 1.5. In 2017, 756 frames of 0.35 s each were taken with average seeing of 1.4. The final images are obtained as the median of all the exposures for each year, after re-centering and rotating the single-exposure images.

2.3. Photometric data

We collected long-term optical photometry of T CrA from the American Association of Variable Star Observers database[1] (AAVSO, Kafka 2020) to investigate its secular evolution. We also considered data acquired within the ASAS (Pojmanski 1997)[2] and ASAS-SN surveys (Shappee et al. 2014)[3]. While these are more accurate than the AAVSO data, they have a much more limited temporal coverage. The results are fully consistent with the long-term light curve obtained from the AAVSO data, but no further insight could be obtained. Thus, we refrain from discussing the ASAS data further in this paper.

2.4. ALMA data

T CrA was observed by ALMA on 2016 August 1–2 (project 2015.1.01058.S). Details of the observations and calibration are described in Cazzoletti et al. (2019). These authors also present an analysis of the continuum emission. For the current paper, the continuum emission was imaged using Hogböm CLEANing with Brigss weighting, a robust parameter of 0.5, and a manually drawn CLEAN mask. The resulting beam size is 0.36 × 0.27 arcsec (PA +78°). The noise level is 0.12 mJy, and a continuum flux of 3.1 mJy is detected. These values are not corrected for the primary beam response, which can be expected

[1] https://www.aavso.org/data-access
[2] http://www.astrouw.edu.pl/asas/?page=aasc&catsrc=asas3
[3] https://asas-sn.osu.edu/variables

to affect the results since the observations was not centered on the target. A 2D Gaussian fit to the continuum emission shows that the continuum emission is slightly resolved, with a size of 0.54×0.37 and a PA of +23°.

The ^{12}CO line emission was imaged using natural weighting and 0.5 km s^{-1} channels, from $V_{\rm LSR}$ = −5 to +15 km s^{-1}; no emission was detected outside this range. We used hand-drawn masks for each individual channel and applied multi-scale CLEAN with scales of 0, 5, 15, and 25 pixels. A pixel scale of 12.251 mas was used, coincident with the SPHERE pixel scale. Because the CrA region contains extended CO emission around the systemic velocity of T CrA (e.g., Cazzoletti et al. 2019), we removed all baselines shorter than 55 kλ. This removed most, but not all, of the extended line flux and also limits the recovered spatial scales to ∼3.75 arcsec.

3. Data analysis

The new and archival data described in the previous section allow us to investigate the nature of T CrA as young stellar object. In this section, we analyze the observational evidence we have for the stellar system, its environment, and the geometry of the extended structures visible in scattered light. In Sect. 3.1, we analyze the clues related to the binarity of the system. In Sect. 3.2, we show the newly acquired polarized light image in H-band of T CrA, describing all the features that we see in the image.

3.1. T CrA as binary system

The light curve (Fig. 2) shows alternate and periodic maxima and minima. The photometric time series analyzed in this study consists of more than 5100 V-band data points collected from the AAVSO database and taken in a period of over 100 yR, between 1910 and 2010. Each point in Fig. 2 is the mean value over each year. The secular evolution of the light curve is well reproduced by a sinusoidal function with a period of 29.6 yr. Sinusoidal light curves, such as the one observed in T CrA, can be due to different effects such as rotation, pulsation, the presence of eclipsing binaries, or occulting binaries. In the case of occulting binaries, the period is generally longer than in the other cases and the occultation is not only due to the stars, but also to the circumstellar disks surrounding one or both stars. The light curve of T CrA is suggestive of the motion of an occulting binary star. The variation (ΔV) in V-magnitude is of the order of ∼1.4 ± 0.2 mag (see Fig. 2).

Evidence of the presence of a binary star is also provided by the peculiar proper motion of T CrA. Indeed, T CrA shows a relative average motion of 7.5 ± 3.8 mas yr^{-1} with respect to the cluster in the direction (PA_{PM}) = 156 ± 30° over the period 1998 (mean epoch of UCAC4 and PPMXL observation) and 2016 (epoch of *Gaia* DR3). These values are given by the difference between the proper motion of T CrA, $\mu_\alpha \cos\delta$ = 4.2 ± 2.5 mas yr^{-1} in RA and μ_δ = −6.2 ± 2.9 mas yr^{-1} in Dec (see Appendix B) and the average proper motion of the on-cloud Coronet cluster members ($\mu_\alpha \cos\delta$ = 4.3 mas yr^{-1} and μ_δ = −27.3 mas yr^{-1}, Galli et al. 2020). This result might indicate a peculiar (large) motion of T CrA with respect to the Coronet cluster. However, the position of T CrA is also constrained and defined by the position of the two associated MHOs (Kumar et al. 2011). We measured the position angle of the straight line connecting MHO 2013 and 2015, which are thought to be connected to the star (Kumar et al. 2011), and crossing T CrA,

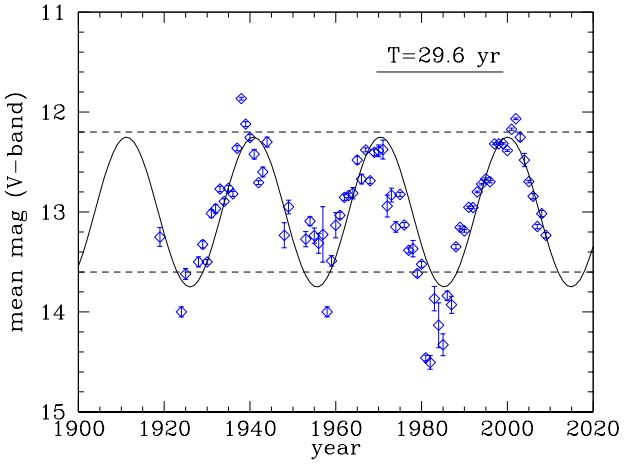

Fig. 2. Secular light curve of T CrA with the photometry collected from the AAVSO archive. Each point is the mean value for each year; the error bar is the standard deviation of the mean. The horizontal dashed lines show the ΔV-mag variation. The period of the light curve that measured as the mean between the difference of the first and third maxima and minima is labeled.

finding the position angle of the bipolar outflow (PA_{MHO}) to be $PA_{MHO} \simeq 33°$. This represents the direction of the large-scale bipolar outflows. We notice that the minimum distance between T CrA and the line connecting the two MHOs is only 0.44″. While this small offset is within the errors in the MHO positions, it can be used to set an upper limit to the relative proper motion of T CrA with the Coronet cloud in the direction perpendicular to this straight line, that is roughly along the direction where we found an offset between the proper motion of T CrA measured above and that of the Coronet cluster. The exact value depends on the time elapsed between the expulsion of the material responsible for the MHO and the observation by Kumar et al. (2011). Given the projected distances from the star of the MHOs are 217″ (MHO 2013) and 64″ (MHO 2015), considering the distance of the Coronet cluster and assuming the collimated fast outflowing gas has a speed of approximately 200 km s^{-1} as typical for jets from young stars (e.g., Frank et al. 2014), we find that the material was expelled 765 yr ago (for MHO2013) and 224 yr ago (for MHO 2015). The upper limit on the proper motion of T CrA with respect to the cloud is then obtained by dividing the measured offset between the barycenter of the system that includes T Cra and the line connecting the two MHOs: the result is about 1 mas yr^{-1}, an order of magnitude less than the offset in proper motions considered above and consistent with the typical scatter of stars in the Coronet cluster. We conclude that this offset is not due to a real peculiar motion of T CrA, which moves as the Coronet cluster, and should then be an apparent or transient effect that might be due to the orbital motion of the central binary star.

Additional evidence of T CrA as a binary system can also be found in the images acquired with IRDIS in 2018 and 2021 and NACO in 2007, 2016, and 2017. We subtracted a median PSF, obtained by rotating and averaging the PSF image in steps of one degree, to the raw NACO images taken in 2007 and 2016–2017. For IRDIS, we used the flux calibration images that are acquired before and after the science sequence. The technique, described by Bonavita et al. (2021), allows us to make a differential image that cancels static aberrations. The output of the procedure is a contrast map that allows to spot stellar companions. Due to the contrast limit and to the limits imposed by the diffraction

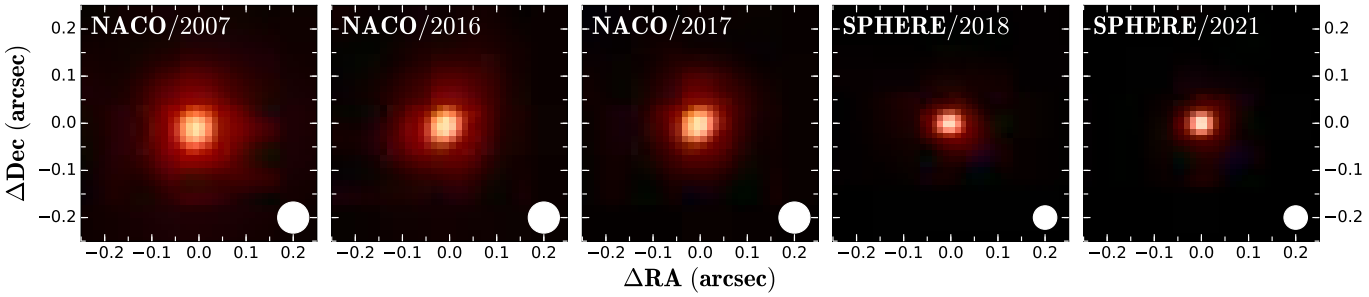

Fig. 3. PSF for all the epochs T CrA was observed. The size of the PSF for every single epochs is shown in the bottom-right corner. For the NACO 2016 and 2017 data sets, we notice an elongation of the PSF in the NW-SE direction.

patterns, none of the images obtained allow us to clearly and uniquely detect the presence of a companion star. However, The PSF of the NACO 2016 and 2017 data set clearly show an extension in the same direction (see Fig. 3), namely NW–SE, but in the NACO 2007 data set we do not see this extension. A slight extension can be seen in the SPHERE 2018 data set, while no extension in the SPHERE 2021 data set. The observed extensions, all in the same direction, are very unlikely to be caused by adaptive optic effect, but might indicate a distortion of the PSF due to an unresolved companion.

3.2. Geometry of the system

Figure 1 shows the polarized light image in H-band of T CrA. The image shows several structures, as annotated. In the right panel, the brightly illuminated top-side of the outer disk is clearly visible, as well as the shielded disk mid-plane, seen as a stark dark lane in approximately the N–S direction. On larger scale, in the middle panel, we can identify two different extended emissions. The extended emission labeled as "feature 1" is two-lobed and extends in the NE–SW direction, up to 2″ from the central source. The extended emission, labeled as "feature 2", appears to be two-lobed as well and it is approximately oriented along the N–S direction. The south lobe extends out to the edge of SPHERE/IRDIS field of view, while the north lobe extends up to ∼5″ from the central source. We analyze these different structures in the following section.

3.2.1. Outer disk

Figure 1 in the right panel shows a very prominent morphological feature composed by a dark lane and a bright region that represents the disk surface. This outer disk appears highly inclined and oriented almost edge-on with respect to the observer, extending almost to the edge of the coronagraph. The dark lane has a maximum width of ∼0.2″ along the E–W direction, corresponding to ∼30 au if it were seen exactly edge-on. Moreover, the disk seen as a dark lane shows an offset with respect to the center of the image that corresponds to ∼10 pixels in the westerly direction (∼122 mas) that is about four times the FWHM of the point spread function. The disk surface is instead shown by the bright regions that extend further out. The PA of the disk measures $PA_{disk} = 7 \pm 2°$, shown as green line in Fig. 1. The disk appears highly inclined and seen as a dark lane, as in the case for DoAr25 (Garufi et al. 2020), MY Lup, and IM Lup (Avenhaus et al. 2018). From the images, we cannot provide a precise estimate of the disk inclination, but we can make a few considerations. The brightness asymmetry between the bright disk top-side and the diffuse disk bottom-side, indicates that the disk is not exactly seen edge-on; indeed, in that case we should expect the top- and bottom-side of the disk to be equally bright. Moreover, the offset between the dark-lane and the center of the image provides another hint of a not-exactly-edge-on disk. From a simple trigonometric consideration, we can measure the inclination of the disk from the angle between the center of the image and the center of the dark lane and dividing for half the lengths of the dark lane, finding an inclination of ∼87°. We can conservatively assume that the T CrA disk, identified as a dark lane in the SPHERE image has an inclination between 85 and 90°. Another possible interpretation for the dark lane could be that it is due to a shadow cast by a highly inclined inner disk close to the center, as in the case of SU Aur (Ginski et al. 2021). However, in this scenario, we cannot reconcile the brightness asymmetry between the bright top-side and the diffuse bottom-side of the disk. Moreover, we should expect the shadow to cross the center of the image, while it appears shifted to the west by ∼10 pixels.

In order to investigate the innermost region of the outer disk, we have plotted the radial profile of the flux seen in Q_Φ scattered light along a slice oriented as the disk, seven pixels wide and 2.5″ long. The radial profile, normalized to the brightness peak of the disk, is shown in Fig. 4 as a black line. The grey area shows the coronagraph. The disk has a gap that extends up to ∼25 au and is quite symmetric in the innermost region. As far as 60 au the disk start to look asymmetric, and extends up to ∼100 au. The observed asymmetry might be due to the outflowing material that overlaps with the disk itself in the north side (as discussed in the next section). From this analysis we consider for the outer disk an inner rim with radius $r_{in} = 0.17''$ (∼25 au) and an outer rim $r_{out} = 0.67''$ (∼100 au). We performed the same analysis of the radial profile in the direction orthogonal to the disk, and shown as blue-dotted line in Fig. 4. On the east side, there is emission from the scattered light down to the border of the coronagraph ($r_{in-east} \lesssim 14$ au) and inside the disk rim measured along the disk direction. As expected, on the west side, the emission starts farther out, due to the presence of the disk's dark silhouette ($r_{in-west} \sim 30$ au). We notice that in the westerly direction at radial distances >50 au there is contamination with the outflowing material. We will discuss the presence of scattered light emission inside the outer disk gap in the following section, showing that it may suggest the presence of an intermediate circumbinary disk surrounding the central binary system.

3.2.2. Extended emission

The structure seen in scattered light in the NE–SW direction (identified as feature 1) is consistent with an outflow in the

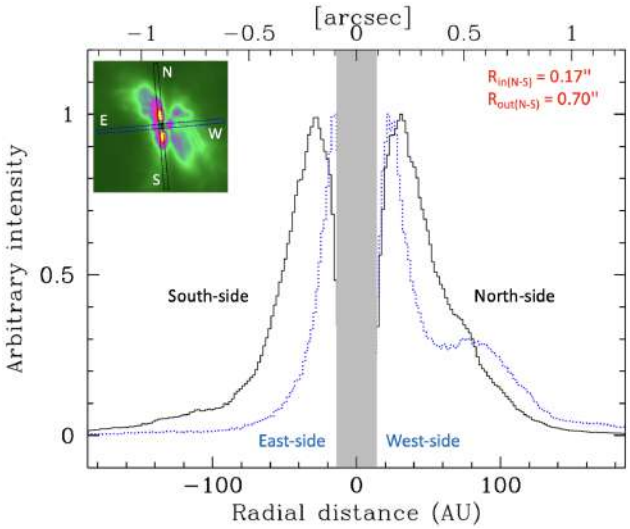

Fig. 4. Radial profile of the Q_ϕ image. The black profile shows the radial profile obtained along a 2.5″ long slice centered on the star in the N–S direction, with PA = 7° and extending along the disk (black-dashed box in the insert). The blue-dotted profile shows the radial profile obtained in the orthogonal direction (E–W, blue-dashed box in the insert). All profiles are normalized to the brightness peak of the disk. The gray area shows the radius of the coronagraph.

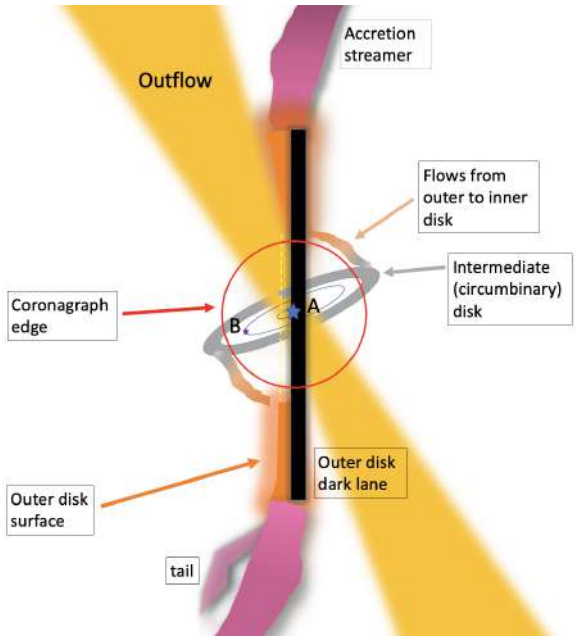

Fig. 5. Cartoon (not to scale) of the proposed model for the T CrA system. All the features seen in the scattered light images are labeled. Moreover, the central binary system and the size of the coronagraph is shown.

direction of the line connecting the two MHOs (MHO2013 and MHO2015) that are unambiguously associated to T CrA (show in the left panel of Fig. 1), which are however at a projected separation of ∼35 000 au and ∼10 000 au, respectively. The presence of the MHOs is a clear sign that the source has in the past already experienced outflowing phenomena, hence, it is consistent to consider the emission seen in scattered light in the same directions as associated to outflowing material close to the star. From a geometrical point of view, the dust seen in scattered light in the direction of the outflow has a position angle of $PA_{outflow}$ ∼35° with a semi-aperture of ∼25°. This is consistent with the PA_{MHO} discussed above.

The extended emission that elongates approximately in the N-S direction (identified as feature 2) is two lobed as well. In the north, it extends up to 4.5″ from the center and appears bent toward the westerly direction. The southern feature (feature 2) extends up to the edge of the field of view and appears brighter than the northern feature. We can also detect a faint dust tail extending from the main disk toward SE. In the case of SU Aur, where several tails are detected (Ginski et al. 2021), we can trace the tail structure until it merges with the disk. Feature 2 is most likely to be showing the presence of accretion streamers that bring material from the forming cloud filament to the outer disk. From the polarized (Fig. 1) and total intensity images of T CrA, we can see that in both cases, the northern streamer is fainter than the southern streamer, indicating that we overall receive more photons from the southern side than from the northern side of the extended structure. Moreover, the ratio between the polarized and total intensity image shows that the overall degree of polarization is similar on both sides. This indicates that light from the south streamer is scattered with angles smaller than 90°, favoring forward scattering. Because the north streamer shows a similar degree of polarization, but an overall fainter signal, we conclude that the light is scattered with angles larger than 90°. Hence, the south streamer is angled toward the observed and the north streamer is angled away from the observer.

4. Discussion

The environment around T CrA is very complex and the analysis of new and archival data shows several features. In the following we discuss each piece of evidence presented in the previous sections and we provide a global picture of its circumstellar environment. A cartoon of the proposed model, showing all the observational evidence analyzed in the previous section, is shown in Fig. 5.

4.1. Modeling of the light curve

Motivated by the light curve, the peculiar proper motion, and the PSF distortion, we conducted a detailed analysis of the photometric and proper motion data with the aim of making a comparison with new information on the system's geometry that is based SPHERE images. In the attempt to reproduce the observed light curve and the H-band magnitude collected from 2MASS, we develop a Monte Carlo (MC) model that accounts for the light emitted from a binary system and partially absorbed by a disk seen edge-on, modeled as a slab with an exponential profile, and inclined with respect to the binary's orbit by 35°, corresponding to an orbit perpendicular to the outflow's direction. In this simplified model, we assume, for the binary system, a circular orbit seen itself edge-on. While the circular orbit is an assumption made to reduce the number of free parameters and, hence, to avoid degeneracy in the models, the high inclination of the binary orbit is supported by the observation. Indeed, as discussed in Pascucci et al. (2020), evidence from the small blueshift of the [OI] and [NeII] forbidden lines of T CrA suggests that the inner disk is itself close to edge-on, with the microjets near to the plane of the sky. We assume for the F0 star, a mass of 1.7 $M_\odot$ for the primary star, corresponding to 2 Myrs from the BHAC evolutionary tracks (Baraffe et al. 2015), along with a circular orbit and a period of 29.6 yr, as found from the light curve. The model provides the mass ratio

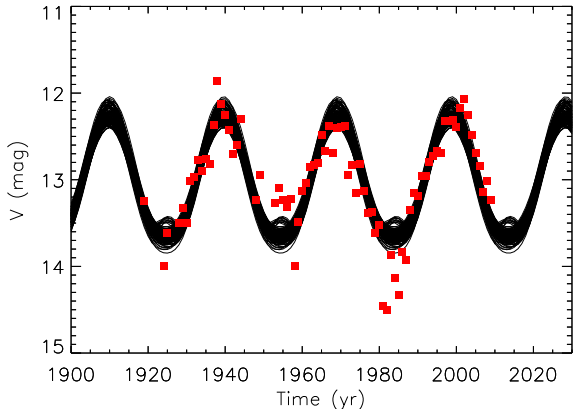

Fig. 6. Light curve of T CrA (red points) compared to the light curves computed with the MC model (black lines) assuming a period of 29.6 yr.

Table 1. Stellar parameters obtained from the modeling of T CrA as a binary star.

Parameters	Value
log(q)	–0.27 ± 0.17 $M_\odot$
T0	2006.06 ± 0.4 yr
AV_0	6.7 ± 1.1 mag
Disk thickness	54.7 ± 20.2 mas
Disk offset	90.7 ± 19.2 mas

Notes. The primary mass star is assumed to be 1.7 $M_\odot$, the orbit to be circular, and with a period of 29.6 yr.

(q) between the primary and secondary component of the binary system, the epoch of the minimum distance between the two components (T_0, in years), the offset of the center of mass with respect to the absorbing slab (disk offset, in mas), the disk thickness (in mas), and the maximum absorption at the disk center (AV_0, in mag). The proper motion between the 1998 and 2016 is also measured for the purposes of a comparison to the apparent proper motion of T CrA. We show a corner plot of the derived quantities in Appendix C. The MC model computes one million random sampling of the priors and provides solutions with reduced $\chi^2 < 2.3$. Figure 6 shows the comparison between the observed secular evolution of T CrA and the light curve obtained from the model. There is a very good agreement between the observed and modeled light curve. The best-fit parameters for each of the computed values, obtained as the median value of all the solutions with χ^2 <2.3, are reported in Table 1. According to this model, T CrA is a binary system, whose primary star is a 1.7 $M_\odot$ star and the secondary is a ∼0.9 $M_\odot$, and it is orbiting with a period of 29.6 yr. The corresponding semi-major axis of the orbit is ∼12 au, seen edge-on, and with the line of nodes of the orbit almost perpendicular to the position angle determined for the outflow. Moreover, we checked the consistency between the apparent motion, as measured from *Gaia* and ground-based facilities, and the one measured by assuming the motion of the modeled binary system. We find that the offset between the two epochs (1998 and 2016) corresponds to 72 ± 26 mas, which is consistent with the value of 130 ± 66 mas measured via *Gaia* and UCAC4/PPMXL observations, hence, justifying the large proper motion of T CrA with respect to the Coronet motion as due to the motion of the binary system. We will further discuss the results from the model in the next section.

4.2. Disk and extended emission

Thanks to the new images acquired with SPHERE/IRDIS and the wealth of literature data on this target, we have now a better knowledge of the disk and extended structure around T CrA, and it appears to be very composite. The disk itself is composed by inner (circumstellar) disk(s) surrounding the primary (secondary) star of the binary system, an intermediate (circumbinary) disk, slightly visible in scattered light, and an outer (circumbinary) disk that is the most prominent in scattered light. Together with the extended emission features, we will discuss all these features in the following subsections.

Disks. The outer disk around T CrA is not continuous. The scattered light images and the radial profile analysis of the Q_Φ image show that the bright top-side of the outer disk extends up to ∼100 au in the N–S direction, and show a gap in the same direction that extends down to ∼25 au.

Evidence of an inner (circumstellar) disk(s) surrounding the primary (secondary) star of the binary system comes from the several tracers of gas and dust well beyond the dust gap. Pascucci et al. (2020) analyzed the [OI] λ6300 and [NeII] 12.81 μm emission lines observed in high-resolution optical and infrared spectra, concluding that they are associated to fast and collimated microjets. In addition, the presence of gas can also be inferred from the non-negligible level of mass accretion rate ($\dot{M}_{\rm acc} \sim 8.1\times10^{-9}$ $M_\odot$ yr^{-1}, Dong et al. 2018; Takami et al. 2003). This gas is most likely distributed into an inner circumstellar disk that allows for accretion onto the system. The presence of the inner disk is also highlighted by mid-infrared interferometric data of the thermal emission of disk (Varga et al. 2018), and by the SED (Sicilia-Aguilar et al. 2013; Sandell et al. 2021).

The images acquired with SPHERE show the presence of scattered light down to the edge of the coronagraph in the E-W direction. The origin of such emission, highly inclined with respect to the outer disk, is not clear. However (as we describe in Sect. 4.4), it might be due to an intermediate circumbinary disk, which is a natural transient consequence of the breaking of the innermost circumstellar disks due to the different inclination of inner and outer disks. Evidence of emission very close to the coronagraph edges are also found by Cugno et al. 2022 using the NaCo imager with the L' filter (λ = 3.6 μm) within the NaCo-ISPY large program.

Feature 1. The PA of the extended emission (identified as feature 1) is consistent with the large-scale MHOs and coincident with the small-scale microjets detected via forbidden lines (Pascucci et al. 2020). Hence, we can reasonably assume that it is representing outflows detected in scattered light and that this feature is orthogonal to the inner and intermediate disk. The innermost disks (inner and intermediate) are misaligned with respect to the outer disk, with a PA for the inner disk of ∼125°, measured as $PA_{\rm outflow}$+90°. Considering the outer disk is seen with $PA_{\rm disk}$ = 7°, the resulting misalignment between innermost and outer disk is on the order of 62°, with an uncertainty of ±10°. This feature is illuminated by the central system. The shape of the outflow is due to higher density regions of dust, generated by instabilities created by two or more layers of material with different densities and velocities resulting in a wind-blown cavity (Liang et al. 2020). The regions with different physical properties are the highly collimated microjet (as seen from the detection of forbidden lines, e.g., Pascucci et al. 2020) and the surrounding wider-angle disk wind, or parent cloud. The impact between these two regions, besides carving out a large and slow massive outflow cavity into the parent cloud (Frank et al. 2014), creates

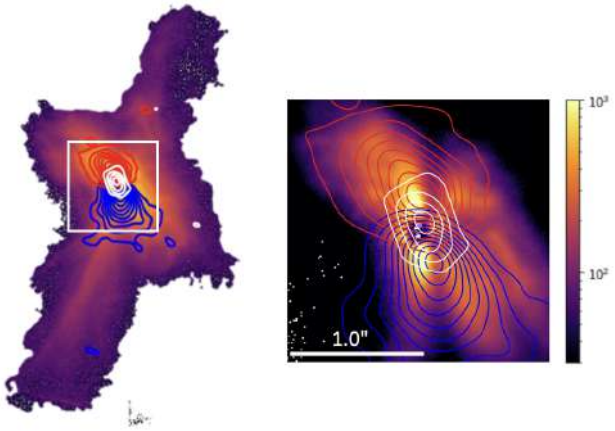

Fig. 7. Overlay of SPHERE (color scale) and ALMA (contours) data. On the left all the extended structure as seen with SPHERE, on the right a zoom-in of the innermost 2″. White contours are ALMA 1.3 mm continuum, plotted at contours starting at, and increasing with, 3σ = 0.37 mJy beam^{-1}. Red and blue contours are integrated ^{12}CO 2–1 emission over 10 km s^{-1} blue- and red-shifted relative to the source velocity, taken as $V_{\rm LSR}$ = 4.5 km s^{-1}. Red and blue contours are also drawn starting at (and increasing with) 3σ = 0.12 Jy beam^{-1} km s^{-1}. The ALMA data are aligned with the SPHERE data to have the stellar position at the center of the image; the continuum emission peaks ∼0.06″ north of that position.

regions of high density where dust grains accumulate, becoming brighter in scattered light. We also notice that there is a good agreement between the small-scale outflow seen in the polarimetric images and the large-scale outflows determined by the MHOs, supporting the scenario of highly collimated jets carving a cavity and creating high-density regions. We also tested the emission seen in scattered light versus the continuum thermal emission at 1.3 mm, and the ^{12}CO emission seen with ALMA. In Fig. 7, we show the continuum emission and the red- and blue-shifted line emission overlayed on the SPHERE scattered light image. The continuum emission, shown as white contours, is slightly resolved, compact, and it is distinctly different from the orientation of the beam. The comparison with the SPHERE image is not quite conclusive in the direction of the emission, if along the disk or the extended emission identified as feature 1. ^{12}CO line emission was clearly detected in the channels, consistent with a structure of ∼2.5 arcsec in diameter. The emission is most likely due to the combination from emission aligned with the disk orientation inferred from SPHERE, and emission from the outflowing material in the same direction as the MHOs. The gas emission close to the N-S direction might trace the gas in the outer disk and the velocity structure of the line emission is consistent with Keplerian rotation. The emission from the outflowing material is in the same direction as the MHOs. The velocities of the extended emission span from −3 to 11 km s^{-1}. The low velocities for the outflowing material confirm that the emission must happen close to the plane of the sky, as was also found by Pascucci et al. (2020). In both cases, either when tracing the outer disk or the outflowing material, the N–E side is receding and the S–W side is approaching the observer.

Misalignment between the inner and the outer disks are not rare. As an example, Bohn et al. (2021) recently investigated a misalignment between the inner and outer disks in transitional disks, finding that out of a sample of 20 objects analyzed, 6 clearly show evidence of misalignment, 5 do not show evidence of misalignment, and the others cannot be evaluated with current data. Misaligned disks, as well as disks whose orientations vary with time, can be the result of their formation taking place in a turbulent, chaotic environment (Bate 2018). Moreover, the evolution of the stellar and disk spin axes during the formation of a star that is accreting in a variable fashion from an inherently chaotic environment might affect the disk orientation as well (Bate et al. 2010). Also, late infalling events, which carry along a specific angular momentum with respect to the star, may tilt the pre-existing disk to another rotation axis depending on the mass ratio of the mass accreted and the disk (Dullemond et al. 2019; Kuffmeier et al. 2021). This was indeed recently observed within the DESTINYS program for the SU Aur system (Ginski et al. 2021), which shows large-scale streamers in scattered light, similar to those observed in our new observations of T CrA and which were shown to trace infalling material. Stellar properties, such as strong stellar magnetic dipole, can cause a warp or misalignment in the innermost region of the disk (e.g., Matsumoto & Tomisaka 2004; Machida et al. 2006; Matsumoto et al. 2006; Hennebelle & Ciardi 2009; Joos et al. 2012; Krumholz et al. 2013; Li et al. 2013; Lewis et al. 2015; Lewis & Bate 2017; Wurster & Li 2018). Additionally, the presence of a companion, either stellar or substellar, can also cause inner and outer disk misalignment (e.g., Facchini et al. 2013, 2018; Zhu 2019; Nealon et al. 2020), as in the case of HD 142527 (Owen & Lai 2017; Price et al. 2018a).

Indeed, T CrA and HD 142527 show several similarities even if the inclinations at which the outer disks are seen are very different (almost edge-on in the case of T CrA and almost face-on for HD 142527). HD 142527 is a binary system characterized by a primary 2.0 $M_\odot$ star surrounded by an inner disk significantly misaligned (59°) with respect to the outer disk (Balmer et al. 2022). For T CrA the outer disk is seen almost edge-on and the misalignment between outer and inner disk is coincident with the inclination of the inner disk orbit, namely ∼55°. The primary star in both cases is an F-type Herbig. In the case of HD 142527 all the main observational features (spirals, shadows seen in scattered light, horseshoe dust structure, radial flows, and streamers) can be explained by the interaction between the disk and the observed binary companion (Price et al. 2018a). The analysis done on HD 142527 led the authors (Price et al. 2018a) to conclude that the disk around this Herbig star is a circumbinary rather than transitional disk, with an inclined inner disk, and with streamers of material connecting the inner and outer disk. In the case of T CrA, if we assume that the inner disk is aligned perpendicular to the outflowing material (and, hence, misaligned with respect to the outer disk), the configuration is similar. Hints of dusty material inside and misaligned with respect to the outer disk come from the radial profile of the scattered light signal seen from SPHERE/IRDIS (shown in Fig. 4), where in the east side of the disk in the direction orthogonal to the disk, there is material present down to the coronagraph edge. However, we cannot say from these images if this material is organized into a disk structure itself or if it represents a streamer of material accreting from the outer disk onto the inner regions of the system. However, as opposite to HD 142527, we must mention the absence of obvious shadowing features in scattered light in T CrA, which can nevertheless be due to the different viewing geometry. In the following section, we present a 3D hydrodynamical model (just as the one developed for HD 142527) to explain the observed features as disk-binary interaction.

Feature 2. The extended emission identified as feature 2 appears very extended and resembles material falling onto the disk as in the case of SU Aur (Ginski et al. 2021). Unfortunately, the strong foreground contamination due to the overall cloud does not allow us to clearly detect the ^{12}CO (2–1), ^{13}CO (2–1),

and $C^{18}O$ (2–1) transitions at distances larger than ∼2.5″; thus, we could not perform a detailed analysis of the kinematics of the material, as done, for example, in the case of SU Aur (Ginski et al. 2021). Indeed, some parts of the CO disk may be missing from from Fig. 7 because the cloud contaminates the signal. Moreover, the large-scale streamers do not show any emission due to the removal of any sensitivity to large-scale emission in the data reduction process. They may exist, but they are very hard to image. The disk may also be more extended than seen here. Hence, we cannot make a conclusive determination of the nature of the extended emission in feature 2. It is highly unlikely that this emission itself stands as an indication of outflowing material (as in feature 1); rather, it may be most likely due to streamers of material falling onto the disk and connecting that very disk to the surrounding cloud material, as is the case for SU Aur. To some extent, we might consider the scattered light morphology of T CrA as an edge-on view of SU Aur, where we can see the streamers of infalling material and at least one tail of accretion. The same streamers of accretion have already been seen, but not interpreted as such, by Ward-Thompson et al. (1985); Clark et al. (2000). Ward-Thompson et al. (1985) used linear polarization mapping of the region in *R*-band and identified a jet-like structure with a projected lengths of 20″ emerging from T CrA, in the direction of, (but pointing away from) R CrA. Clark et al. (2000) performed near-infrared linear imaging polarimetry in the *J*, *H*, and *Kn* bands, along with circular imaging polarimetry in the *H* band, and interpreted the images as bipolar cavities, where the SE emission is visible as far as ∼15″ from T CrA. These authors stress the presence of a pronounced asymmetry in the polarized intensity images, suggestive of a fairly sudden depolarization of the dust grains caused by foreground material in the reflection nebula. The identification of the MHOs and the analysis of the images acquired with NACO and SPHERE is now showing that the features observed in the past were not associated with jets but more likely the same streamer of accretion seen in scattered light. A possible test for ascertaining the origin of feature 2 can be done using the SO_2 transition from ALMA. Garufi et al. (2022) have indeed shown that for the source IRAS 04302+2247, the SO_2 emission does not probe the disk region, but rather originates at the intersection between extended streamers and disks. We notice that the presence of streamers of material feeding the disk of T CrA would also go in the direction of mitigating the issue of the low disk masses found in CrA. Indeed, it was found that the average disk mass in CrA is significantly lower than that of disks in other young (1–3 Myr) star-forming regions (Lupus, Taurus, Chamaeleon I, and Ophiuchus, Cazzoletti et al. 2019). If there is accretion of fresh material onto the disk, it is possible that we would have lower measured disk masses at the beginning and mitigate the issue (Manara et al. 2018). The observed increase in disk masses with time (e.g., Testi et al. 2022; Cazzoletti et al. 2019) should otherwise be explained with other mechanisms such as planetesimal collisions (Bernabò et al. 2022).

Moreover, the presence of streamers of accretion is also in agreement with the orientation of T CrA with respect to R CrA, both belonging to the Coronet Cluster. These two stars formed within the same filament, which is oriented at PA = 124° projected on sky (this is also the PA of T CrA relative to R CrA). This orientation is indeed similar to that of the orbit proposed for the central binary of T CrA and very close to perpendicular to the PA of the MHO objects (PA = 33°); these values are fully consistent with the direction of the same structures seen in the neighboring star R CrA (Rigliaco et al. 2019; Mesa et al. 2019). This suggests that the bulk of the inflow of material that formed the T CrA system was coplanar with this filament and that the original disk of T CrA was likely oriented at the PA of the filament; this is actually the case for the disk around R CrA as well. However, the current outer disk of T CrA has a very different orientation (PA = 7 degree), although it seems to still be fed by the same filament. This is because T CrA appears to be presently offset by a few hundreds au (a few arcsec on sky) with respect to the filament. Considering the age of T CrA (likely 1–3 Myr), this offset is indeed very small, corresponding to a minuscule velocity of only ∼1 m s^{-1}. This suggests that the generation of a misaligned structure very likely takes place whenever accretion onto the disk is prolonged over such extended intervals of time.

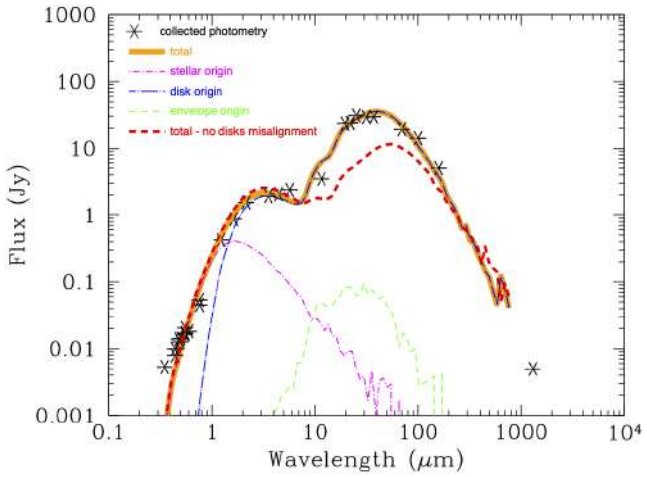

Fig. 8. SED of TCrA. Black asterisks show the published photometry as reported in Table 2. The orange curve shows the total emission. Magenta line shows the SED component due to stellar origin, in blue the component due to the disk, and in green the component due to the envelope. The red curve shows the emission if no misalignment between the intermediate and outer disk is assumed. The oscillations in the model curves at the longest wavelengths are artifacts related to the finite number of photon packets considered in the Monte Carlo scheme.

4.3. Spectral energy distribution

We modeled the SED of T CrA using the dust radiative transfer model developed by Whitney et al. (2003b,a). The code uses a Monte Carlo radiative transfer scheme that follows photon packets emitted by the central star as they are scattered, absorbed, and re-emitted throughout the disk. For the modeling process, we assumed that the geometry of the star+disk system is comprised by a central 2.0 $M_\odot$ source emitting photons and a gapped and misaligned circumstellar disk (as described above). The total mass of the disk, $M_{\rm disk} = 10^{-3} M_\odot$ is in agreement with the $M_{\rm dust}$ value retrieved by Cazzoletti et al. (2019), using the 1.3 mm continuum flux, assuming an interstellar (ISM) gas-to-dust ratio of 100. The outcome of the model, shown in orange in Fig. 8, well reproduces the observed photometric points collected in Table 2, suggesting that the interpretation of inner and outer disks misaligned with respect to one another is in very good agreement with the collected photometry[4]. For comparison, we also show the SED obtained with the same parameters in the case where no misalignment between inner and outer disk is assumed (red profile). In this case, the curve does not adequately reproduce the observed photometry at wavelengths longer than ∼10–15 μm.

[4] The apparent oscillations of the model at wavelengths longer than 300 μm is due to low number statistics and has no physical meaning.

Table 2. Fluxes at different wavelengths collected from the literature used for the SED.

λ_c (μm)	Flux (Jy)	Facility	Reference
0.349	0.00531	SkyMapper	Wolf et al. (2018)
0.444	0.00792	CTIO	Henden et al. (2016)
0.444	0.00988	UCAC4-RPM	Nascimbeni et al. (2016)
0.482	0.0138	CTIO	Henden et al. (2016)
0.497	0.0126	SkyMapper	Wolf et al. (2018)
0.504	0.0142	*Gaia*	Gaia Collaboration (2020)
0.554	0.0163	Hamilton	Herbig & Bell (1988)
0.554	0.0171	CTIO	Henden et al. (2016)
0.554	0.0204	UCAC4-RPM	Nascimbeni et al. (2016)
0.604	0.0181	SkyMapper	Wolf et al. (2018)
0.762	0.045	*Gaia*	Gaia Collaboration (2020)
0.763	0.0539	CTIO	Henden et al. (2016)
1.24	0.425	2MASS-J	Cutri et al. (2003)
1.65	0.871	2MASS-H	Cutri et al. (2003)
2.16	1.55	2MASS-K	Cutri et al. (2003)
3.55	1.93	*Spitzer*/IRAC	Gutermuth et al. (2009)
4.49	2.07	*Spitzer*/IRAC	Gutermuth et al. (2009)
5.73	2.38	*Spitzer*/IRAC	Gutermuth et al. (2009)
11.6	3.48	WISE/W3	Cutri & et al. (2012)
19.7	23.4	SOFIA	Sandell et al. (2021)
22.1	23.8	WISE/W4	Cutri & et al. (2012)
25.3	30.7	SOFIA	Sandell et al. (2021)
31.5	29.0	SOFIA	Sandell et al. (2021)
37.1	29.3	SOFIA	Sandell et al. (2021)
70.0	19.3	*Herschel*	Herschel Group et al. (2020)
100.0	14.2	*Herschel*	Herschel Group et al. (2020)
160.0	5.0	*Herschel*	Herschel Group et al. (2020)
1300	0.00499	ALMA	Cazzoletti et al. (2019)

We must note that the radiative transfer model does not account for the binary star; hence, it may cause deviation in the illumination of the disk. In particular, in their orbit the two stars spend time above the disk midplane, thus illuminating the circumbinary disk from above. In the two SEDs shown in Fig. 8, we do not account for this effect.

4.4. Hydrodynamical simulation

We performed a 3D hydrodynamical simulation of the T CrA configuration considered in this work using the Smoothed Particle Hydrodynamics (SPH) code PHANTOM (Price et al. 2018b; Monaghan 2005; Price 2012). The initial conditions of the system are set following the observational constraints acquired so far. T CrA is modeled as a binary system with masses 1.7 $M_\odot$, and 1.0 $M_\odot$ for the primary and secondary component, respectively. Each star was simulated as a sink particle (Price et al. 2018b; Bate et al. 1995) with an accretion radius of 0.5 au. The orbit is eccentric and the period of the binary star is 29.6 yr, corresponding to a semi-major axis of 13.3 au. The orbit is seen edge-on with an inclination of 90° and PA_{orbit} is perpendicular to the outflowing material (PA_{orbit} = 145°). The outer disk, extending from R_{in} = 25 au to R_{out} = 100 au, was simulated with 8×10^5 SPH particles, resulting in a smoothing length ≈0.2 times the disk scale height. The inner disk, extending from r_{in} = 1 au to r_{out} = 5 au, and co-planar to the orbit of the binary star, was simulated with 2×10^5 SPH particles, resulting in a smoothing length of about the disk scale height. Outflows and inflows were not considered in this model. Viscosity is implemented with the artificial viscosity method (Lucy 1977; Gingold & Monaghan 1977) that results in an Shakura & Sunyaev (1973) α-viscosity, as shown by Lodato & Price (2010). We used $\alpha \approx 5 \times 10^{-3}$. We ran the full hydrodynamical model (with both the outer and the inner disk) for 100 binary orbits in order to relax the initial condition and to produce a synthetic image of the system to compare with the observations. To perform a direct comparison with observations of T CrA, we post-processed our simulation using the Monte Carlo radiative transfer code MCFOST (Pinte et al. 2016) in order to produce synthetic images of the hydrodynamical model. MCFOST maps the physical quantities in the SPH simulation (e.g., dust and gas density, temperature) onto a Voronoi mesh directly built around the SPH particles, without interpolation. We adopted a gas-to-dust mass ratio equal to 100 and we assumed micrometer grains to be well coupled with the gas. These grains scatter the stellar light collected by SPHERE and are assumed to be spherical and homogeneous (as in the Mie theory). Their chemical composition is 60% astronomical silicates and 15% amorphous carbons (as DIANA standard dust composition, Woitke et al. 2016), with a porosity of 10%. The gas mass was directly taken from the SPH simulation. We used the same distance from the source used in this paper (149.4 pc) and ≈10^6 photon packets to compute the temperature profile of the model, plus ≈10^{10} photon packets, to compute the source function of the model in order to produce the scattered light image at 2 μm wavelength.

The total intensity polarized light image obtained with the hydrodynamical simulation is shown in the left panel of Fig. 9. The middle panel is the synthetic image convolved to the SPHERE/IRDIS resolution and in the right panel we show the observed image. There are a few features that are clearly reproduced in the simulation: the dark lane, the offset of the dark lane with respect to the center of the image, and the top-surface of the disk brighter than the bottom-side of the disk. There are two bright spots in the E–W direction on the convolved synthetic image, that are also observed in the real image. These points are due to the intermediate circumbinary disk that breaks from the outer regions, precessing as a rigid body, and leading to its evolution. The breaking of the inner disk generates an intermediate disk that is visible as bright spots at the east and west sides of the coronagraph. We must note that the simulation does not take into consideration the outflowing material and does not account for the replenishment of the outer disk due to the accretion streamers (thus, slowing down its expansion). A more detailed simulation is needed for T CrA, but it is beyond the scope of this observational paper and will be discussed in a separate publication.

In order to measure how the circumbinary disk mass is distributed among the binary stars, we ran a second hydrodynamical model as the one described above, but without the circumprimary disk. Indeed, accretion into a binary system happens via the formation of up to three disks (two circumstellar disks, namely, one around each component, and a circumbinary disk, Monin et al. 2007). The two circumstellar disks are periodically replenished by accretion streamers pulled from the inner edge of the circumbinary disks by the stars (Artymowicz & Lubow 1994; Tofflemire et al. 2017). In a quasi-steady state regime, the mass flux entering the Roche lobe of a star via the gas streamers equals the star accretion rate. Thus, we can reliably measure the fraction of mass accreted onto a star by simulating only the circumbinary disk, provided that the stellar Roche lobes are resolved by the simulation and the central part of the disk has relaxed (as

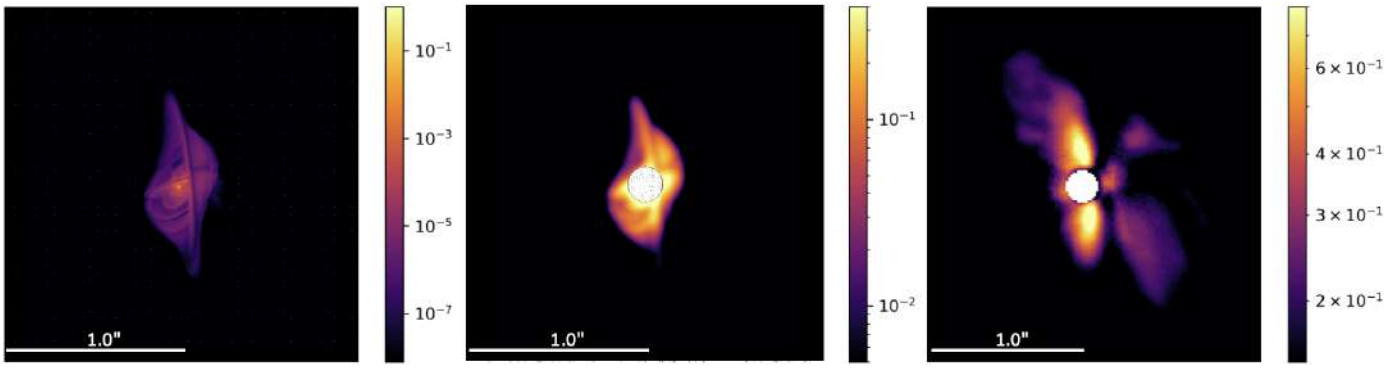

Fig. 9. Snapshot of the SPH simulation compared to the observed image. The left panel shows the result in total intensity of the SPH simulation, with a resolution of 4.0 mas pixel^{-1}. In the middle panel, the same image convolved to the SPHERE/IRDIS resolution (12.25 mas pixel^{-1}). On the right, the observed total intensity image. All images have a 2″ field of view.

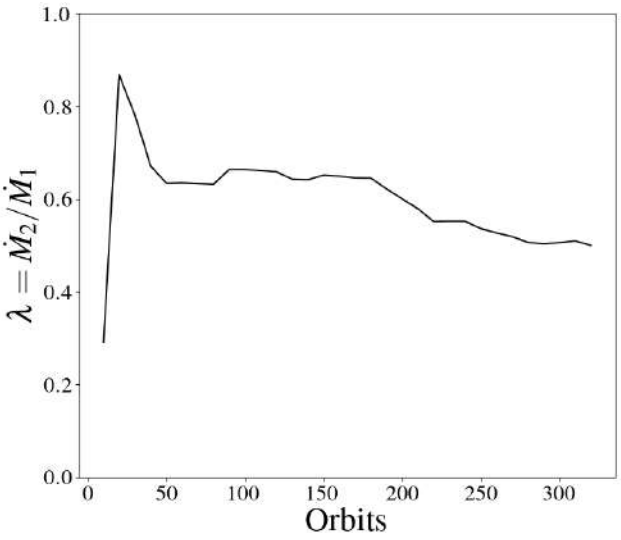

Fig. 10. Mass accretion rate ratio of secondary and primary star as a function of the number of orbits.

done with SPH simulations, e.g., in Young & Clarke 2015 and recently tested in Ceppi et al. 2022). In general, simulations of accretion into binary systems find that the primordial mass ratio is pushed towards unity (that is, closer to equal masses in the binary components) by accretion from a circumbinary disk (Clarke 2012). This is due to the ease with which the secondary component accretes the infalling gas, as it lies farther from the binary barycenter and closer to the disk edge. Its differential velocity with respect to the gas is also low, allowing it to accrete efficiently. In the case of T CrA, the primary star is still accreting more than the secondary (see Fig. 10). This is due to the misalignment between inner and outer disk that makes the secondary to be at considerable height over or below the disk for a large fraction of its orbit.

5. Summary and conclusions

We investigated new and archival data of the Herbig Ae/Be star T CrA collected with different instruments. The analysis of the data shows that T CrA is a very interesting and complex system, belonging to one of the nearest and most active region of star formation. Combining archival NACO imaging data with photometric data, along with new and archival SPHERE adaptive optics images, we were able to study the complex stellar environment around T CrA and the stellar properties. Our conclusions are as follows:

- The outer disk is seen edge-on as a dark lane elongated approximately in the N–S. The dark lane is shifted by 122 mas with respect to the center of the image and it is seen with a PA of 7°. This value is in very good agreement with the value recently found by Cugno et al. (2022) using a different instrument and data set;
- The bright illuminated top-side of the disk surface is clearly visible in scattered light;
- Extended emission in the NE–SW direction, identified as feature 1, is consistent in its direction with the line connecting the two-lobed MHOs seen on a larger scale. It is most likely outflowing material, with PA = 33°, consistent with the PA of the two MHOs.
- Extended emission in the N-S direction, identified as feature 2, is interpreted as large-scale streamers of material likely infalling onto the disk. In the north, the streamer extends up to ∼4.5″ from the central system, while in the south, it extends up to the edge of the field of view, and probably beyond, as suggested by previous stellar polarization images in the optical and NIR;
- The periodic behavior of the light curve suggests a central binary with a period of 29.6 yr. Even if the non-coronagraphic images acquired with NACO and SPHERE do not show direct evidence of the presence of a stellar companion, a detailed comparison of the position of the secondary along the proposed orbit at the epochs of the observations (acquired so far with NACO and SPHERE) shows that in all of them, the target was too close to the primary star for detection as a separate object. According to our modeling results, the two components will be at their maximum separation in 2027. At that time, appropriate high-contrast images at that epoch should provide direct evidence of the binary system.

Overall, we find that the binary system and intermediate circumbinary disk lay on different geometrical planes, placing T CrA among the objects with a misaligned inner disk. Inner and outer disk misalignment is not rare and in very recent years, thanks to high-contrast imaging, it is becoming clear that the misalignment can also be due to the accretion history of the star-forming cloud onto the disk. Indeed in the case of T CrA (as well as SU Aur), we found evidence of the presence of streamers of accreting material that connect the filament along which the star has formed with the outer part of the disk. These streamers have an angular momentum with respect to the star whose direction is

very different from that of the system (in the case of T CrA, this is dominated by the binary) causing a misalignment between an inner and outer disk.

Besides characterizing the disk and outflow structures around T CrA, we have also modeled its spectral energy distribution, showing that the disk geometry obtained is fully consistent with the observed SED and such a consistency is not reached if we do not consider the misalignment between inner and outer disk. Moreover, we performed a hydrodynamical simulation of the configuration for 100 orbits of the binary star. The model is consistent with the observations and the analysis of the accretion rates of the individual stars shows that the accretion happens mainly onto the primary star, rather than on the secondary, as a consequence of the inclination between the inner, intermediate, and outer disks. Also, the light curve is easily explained assuming the configuration of two misaligned disks. A comparison of the ALMA continuum and ^{12}CO emission was also performed. While for the continuum emission we cannot clearly point out the region where the dust is located – if it is indeed along the disk or the outflowing material, the gas emission is most likely due to the combination from emission aligned with the disk orientation (inferred from SPHERE) and emission from the outflowing material in the same direction as the MHOs.

The analysis conducted on T CrA has confirmed its extremely interesting and complex nature. As in the case of HD142527, the misalignment between inner and outer disk can be due to the interaction between the disk and the central binary system. On the other hand, the large-scale streamers observed in the N–S direction are very similar to the disk-cloud interaction observed for SU Aur, which represents material infalling onto the disk, – and the inner and outer disk misalignment might be caused by this interaction. The need for high-resolution observations to disentangle the different effects that shape early planetary system formation is clear. Overall, T CrA is an excellent target and laboratory that can help improve our understanding of the impact of binarity and the environment in the evolution of protoplanetary disks.

Acknowledgements. We would like to thank the referee Roubing Dong, whose careful and constructive comments improved the quality of this manuscript. E.R. was supported by the European Union's Horizon 2020 research and innovation programme under the Marie Skłodowska-Curie grant agreement No 664931. This work has been supported by the project PRIN INAF 2016 The Cradle of Life – GENESIS-SKA (General Conditions in Early Planetary Systems for the rise of life with SKA) and by the "Progetti Premiali" funding scheme of the Italian Ministry of Education, University, and Research. C.F.M. acknowledges funding from the European Union under the European Union's Horizon Europe Research & Innovation Programme 101039452 (WANDA). Views and opinions expressed are however those of the author(s) only and do not necessarily reflect those of the European Union or the European Research Council. Neither the European Union nor the granting authority can be held responsible for them. T.B. acknowledges funding from the European Research Council (ERC) under the European Union's Horizon 2020 research and innovation programme under grant agreement No 714769 and funding by the Deutsche Forschungsgemeinschaft (DFG, German Research Foundation) under grants 361140270, 325594231, and Germany's Excellence Strategy – EXC-2094 – 390783311. A.R. has been supported by the UK Science and Technology research Council (STFC) via the consolidated grant ST/S000623/1 and by the European Union's Horizon 2020 research and innovation programme under the Marie Sklodowska-Curie grant agreement No. 823823 (RISE DUSTBUSTERS project). This paper makes use of the following ALMA data: ADS/JAO.ALMA#2016.0.01058.S. ALMA is a partnership of ESO (representing its member states), NSF (USA) and NINS (Japan), together with NRC (Canada), MOST and ASIAA (Taiwan), and KASI (Republic of Korea), in cooperation with the Republic of Chile. The Joint ALMA Observatory is operated by ESO, AUI/NRAO and NAOJ. M.R.H. acknowledges the assistance of Allegro, the ARC node in the Netherlands, who assisted with the calibration of this data set. This work is partly based on data products produced at the SPHERE Data Centre hosted at OSUG/IPAG, Grenoble. We thank P. Delorme and E. Lagadec (SPHERE Data Centre) for their efficient help during the data reduction process. SPHERE is an instrument designed and built by a consortium consisting of IPAG (Grenoble, France), MPIA (Heidelberg, Germany), LAM (Marseille, France), LESIA (Paris, France), Laboratoire Lagrange (Nice, France), INAF Osservatorio Astronomico di Padova (Italy), Observatoire de Genève (Switzerland), ETH Zurich (Switzerland), NOVA (Netherlands), ONERA (France) and ASTRON (Netherlands) in collaboration with ESO. SPHERE was funded by ESO, with additional contributions from CNRS (France), MPIA (Germany), INAF (Italy), FINES (Switzerland) and NOVA (Netherlands). SPHERE also received funding from the European Commission Sixth and Seventh Framework Programmes as part of the Optical Infrared Coordination Network for Astronomy (OPTICON) under grant number RII3-Ct-2004-001566 for FP6 (2004-2008), grant number 226604 for FP7 (2009-2012), and grant number 312430 for FP7 (2013-2016). This work has made use of data from the European Space Agency (ESA) mission *Gaia* (`https://www.cosmos.esa.int/gaia`), processed by the *Gaia* Data Processing and Analysis Consortium (DPAC, `https://www.cosmos.esa.int/web/gaia/dpac/consortium`). Funding for the DPAC has been provided by national institutions, in particular the institutions participating in the *Gaia* Multilateral Agreement. We acknowledge with thanks the variable star observations from the AAVSO International Database contributed by observers worldwide and used in this research.

References

Artymowicz, P., & Lubow, S. H. 1994, ApJ, 421, 651
Avenhaus, H., Quanz, S. P., Garufi, A., et al. 2018, ApJ, 863, 44
Bailey, J. 1998, MNRAS, 301, 161
Balmer, W. O., Follette, K. B., Close, L. M., et al. 2022, ApJ, 164, 29
Baraffe, I., Homeier, D., Allard, F., & Chabrier, G. 2015, A&A, 577, A42
Bate, M. R. 2018, MNRAS, 475, 5618
Bate, M. R., Bonnell, I. A., & Price, N. M. 1995, MNRAS, 277, 362
Bate, M. R., Lodato, G., & Pringle, J. E. 2010, MNRAS, 401, 1505
Bernabò, L. M., Turrini, D., Testi, L., Marzari, F., & Polychroni, D. 2022, ApJ, 927, L22
Beuzit, J. L., Vigan, A., Mouillet, D., et al. 2019, A&A, 631, A155
Bohn, A. J., Benisty, M., Perraut, K., et al. 2022, A&A, 658, A183
Bonavita, M., Gratton, R., Desidera, S., et al. 2022, A&A, 663, A144
Cazzoletti, P., Manara, C. F., Liu, H. B., et al. 2019, A&A, 626, A11
Ceppi, S., Cuello, N., Lodato, G., et al. 2022, MNRAS, 514, 906
Clark, S., McCall, A., Chrysostomou, A., et al. 2000, MNRAS, 319, 337
Clarke, C. J. 2012, IAU Symp., 282, 409
Cugno, G., Pearce, T. D., Launhardt, R., et al. 2022, A&A, 669, A145
Cutri, R. M., et al. 2012, VizieR Online Data Catalog: II/311
Cutri, R. M., Skrutskie, M. F., van Dyk, S., et al. 2003, 2MASS All Sky Catalog of point sources
Davis, C. J., Gell, R., Khanzadyan, T., Smith, M. D., & Jenness, T. 2010, A&A, 511, A24
de Boer, J., Langlois, M., van Holstein, R. G., et al. 2020, A&A, 633, A63
Delorme, P., Meunier, N., Albert, D., et al. 2017, in SF2A-2017: Proceedings of the Annual meeting of the French Society of Astronomy and Astrophysics, ed. C. Reylé, P. Di Matteo, F. Herpin, et al.
Dohlen, K., Langlois, M., Saisse, M., et al. 2008, Proc. SPIE Conf. Ser., 7014, 70143L
Dong, R., Najita, J. R., & Brittain, S. 2018, ApJ, 862, 103
Dullemond, C. P., Küffmeier, M., Goicovic, F., et al. 2019, A&A, 628, A20
Dzib, S. A., Loinard, L., Ortiz-León, G. N., Rodríguez, L. F., & Galli, P. A. B. 2018, ApJ, 867, 151
Facchini, S., Lodato, G., & Price, D. J. 2013, MNRAS, 433, 2142
Facchini, S., Juhász, A., & Lodato, G. 2018, MNRAS, 473, 4459
Frank, A., Ray, T. P., Cabrit, S., et al. 2014, in Protostars and Planets VI, eds. H. Beuther, R. S. Klessen, C. P. Dullemond, & T. Henning (Tucson: University of Arizona Press), 451
Gaia Collaboration 2020, VizieR Online Data Catalog: I/350
Gaia Collaboration (Prusti, T., et al.) 2016, A&A, 595, A1
Gaia Collaboration (Brown, A. G. A., et al.) 2021, A&A, 649, A1
Galli, P. A. B., Bouy, H., Olivares, J., et al. 2020, A&A, 634, A98
Garufi, A., Avenhaus, H., Pérez, S., et al. 2020, A&A, 633, A82
Garufi, A., Podio, L., Codella, C., et al. 2022, A&A, 658, A104
Ghez, A. M., McCarthy, D. W., Patience, J. L., & Beck, T. L. 1997, ApJ, 481, 378
Gingold, R. A., & Monaghan, J. J. 1977, MNRAS, 181, 375
Ginski, C., Ménard, F., Rab, C., et al. 2020, A&A, 642, A119
Ginski, C., Facchini, S., Huang, J., et al. 2021, ApJ, 908, L25
Gutermuth, R. A., Megeath, S. T., Myers, P. C., et al. 2009, ApJS, 184, 18
Henden, A. A., Templeton, M., Terrell, D., et al. 2016, VizieR Online Data Catalog: II/336
Hennebelle, P., & Ciardi, A. 2009, A&A, 506, L29
Herbig, G. H. 1960, ApJS, 4, 337

Herbig, G. H., & Bell, K. R. 1988, Third Catalog of Emission-Line Stars of the Orion Population : 3 : 1988
Herczeg, G. J., & Hillenbrand, L. A. 2014, ApJ, 786, 97
Herschel Group, Marton, G., Calzoletti, L., et al. 2020, VizieR Online Data Catalog VIII/106
Herter, T. L., Adams, J. D., Gull, G. E., et al. 2018, J. Astron. Instrum., 7, 1840005
Joos, M., Hennebelle, P., & Ciardi, A. 2012, A&A, 543, A128
Joy, A. H. 1945, ApJ, 102, 168
Kafka, S. 2020, in European Planetary Science Congress, EPSC2020–314
Köhler, R., Neuhäuser, R., Krämer, S., et al. 2008, A&A, 488, 997
Krumholz, M. R., Crutcher, R. M., & Hull, C. L. H. 2013, ApJ, 767, L11
Kuffmeier, M., Dullemond, C. P., Reissl, S., & Goicovic, F. G. 2021, A&A, 656, A161
Kumar, M. S. N., Sharma, S., Davis, C. J., Borissova, J., & Grave, J. M. C. 2011, A&A, 533, A137
Lenzen, R., Hartung, M., Brandner, W., et al. 2003, SPIE Conf. Ser., 4841, 944
Lewis, B. T., & Bate, M. R. 2017, MNRAS, 467, 3324
Lewis, B. T., Bate, M. R., & Price, D. J. 2015, MNRAS, 451, 288
Li, H.-b., Fang, M., Henning, T., & Kainulainen, J. 2013, MNRAS, 436, 3707
Liang, L., Johnstone, D., Cabrit, S., & Kristensen, L. E. 2020, ApJ, 900, 15
Lindberg, J. E., & Jørgensen, J. K. 2012, A&A, 548, A24
Lodato, G., & Price, D. J. 2010, MNRAS, 405, 1212
Lucy, L. B. 1977, AJ, 82, 1013
Machida, M. N., Matsumoto, T., Hanawa, T., & Tomisaka, K. 2006, ApJ, 645, 1227
Maire, A.-L., Langlois, M., Dohlen, K., et al. 2016, SPIE Conf. Ser., 9908, 990834
Manara, C. F., Morbidelli, A., & Guillot, T. 2018, A&A, 618, L3
Marois, C., Lafrenière, D., Doyon, R., Macintosh, B., & Nadeau, D. 2006, ApJ, 641, 556
Matsumoto, T., & Tomisaka, K. 2004, ApJ, 616, 266
Matsumoto, T., Nakazato, T., & Tomisaka, K. 2006, ApJ, 637, L105
Mendigutía, I., Eiroa, C., Montesinos, B., et al. 2011, A&A, 529, A34
Mesa, D., Bonnefoy, M., Gratton, R., et al. 2019, A&A, 624, A4
Meyer, M. R., & Wilking, B. A. 2009, PASP, 121, 350
Monaghan, J. J. 2005, Rep. Prog. Phys., 68, 1703
Monin, J. L., Clarke, C. J., Prato, L., & McCabe, C. 2007, in Protostars and Planets V, eds. B. Reipurth, D. Jewitt, & K. Keil (Tucson: University of Arizona Press), 395
Nascimbeni, V., Piotto, G., Ortolani, S., et al. 2016, MNRAS, 463, 4210
Nealon, R., Cuello, N., & Alexander, R. 2020, MNRAS, 491, 4108
Owen, J. E., & Lai, D. 2017, MNRAS, 469, 2834
Pascucci, I., Banzatti, A., Gorti, U., et al. 2020, ApJ, 903, 78
Pikhartova, M., Long, Z. C., Assani, K. D., et al. 2021, ApJ, 919, 64
Pinte, C., Dent, W. R. F., Ménard, F., et al. 2016, ApJ, 816, 25
Pojmanski, G. 1997, Acta Astron., 47, 467
Pontoppidan, K. M., Blake, G. A., & Smette, A. 2011, ApJ, 733, 84
Price, D. J. 2012, J. Comput. Phys., 231, 759
Price, D. J., Cuello, N., Pinte, C., et al. 2018a, MNRAS, 477, 1270
Price, D. J., Wurster, J., Tricco, T. S., et al. 2018b, PASA, 35, e031
Rigliaco, E., Gratton, R., Mesa, D., et al. 2019, A&A, 632, A18
Roeser, S., Demleitner, M., & Schilbach, E. 2010, AJ, 139, 2440
Rousset, G., Lacombe, F., Puget, P., et al. 2003, SPIE Conf. Ser., 4839, 140
Sandell, G., Reipurth, B., Vacca, W. D., & Bajaj, N. S. 2021, ApJ, 920, 7
Shakura, N. I., & Sunyaev, R. A. 1973, IAU Symp., 55, 155
Shappee, B. J., Prieto, J. L., Grupe, D., et al. 2014, ApJ, 788, 48
Sicilia-Aguilar, A., Henning, T., Kainulainen, J., & Roccatagliata, V. 2011, ApJ, 736, 137
Sicilia-Aguilar, A., Henning, T., Linz, H., et al. 2013, A&A, 551, A34
Siess, L., Dufour, E., & Forestini, M. 2000, A&A, 358, 593
Takami, M., Bailey, J., & Chrysostomou, A. 2003, A&A, 397, 675
Testi, L., Natta, A., Manara, C. F., et al. 2022, A&A, 663, A98
Tofflemire, B. M., Mathieu, R. D., Ardila, D. R., et al. 2017, ApJ, 835, 8
van Holstein, R. G., Girard, J. H., de Boer, J., et al. 2020, A&A, 633, A64
Varga, J., Ábrahám, P., Chen, L., et al. 2018, A&A, 617, A83
Ward-Thompson, D., Warren-Smith, R. F., Scarrott, S. M., & Wolstencroft, R. D. 1985, MNRAS, 215, 537
Whitney, B. A., Wood, K., Bjorkman, J. E., & Cohen, M. 2003a, ApJ, 598, 1079
Whitney, B. A., Wood, K., Bjorkman, J. E., & Wolff, M. J. 2003b, ApJ, 591, 1049
Woitke, P., Min, M., Pinte, C., et al. 2016, A&A, 586, A103
Wolf, C., Onken, C. A., Luvaul, L. C., et al. 2018, PASA, 35, e010
Wurster, J., & Li, Z.-Y. 2018, Front. Astron. Space Sci., 5, 39
Young, M. D., & Clarke, C. J. 2015, MNRAS, 452, 3085
Zacharias, N., Finch, C. T., Girard, T. M., et al. 2012, VizieR Online Data Catalog: I/322A
Zhu, Z. 2019, MNRAS, 483, 4221

Appendix A: SPHERE polarimetric images

In Figure A.1, we present the Stokes Q and U, as well as the derived Q_Φ and U_Φ images of T CrA. The flux calibration was carried out by measuring the flux of the central star in the non-coronagraphic flux calibration images, taken at the beginning and end of the observation sequence. To convert pixel counts to physical units we used the 2MASS H-band magnitude of the star.

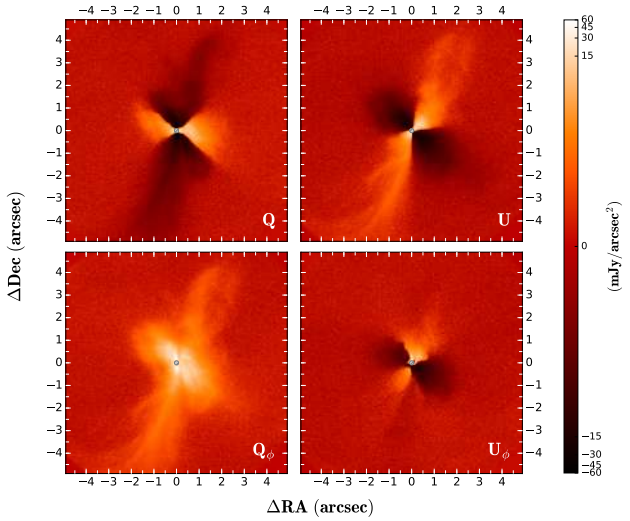

Fig. A.1: Flux-calibrated image of the Q, U, Q_Φ and U_Φ frames.

Appendix B: Proper motion analysis

The average proper motion for the on-cloud Coronet cluster members obtained using Gaia DR2 data from Galli et al. 2020, is $\mu_\alpha \cos\delta$ = 4.3 mas yr^{-1} and μ_δ=-27.3 mas yr^{-1}, with a small dispersion of less than 1 mas/yr for the individual objects. As we mentioned in the introduction, Gaia does not provide astrometric solutions and proper motion for the star T CrA. However, we can check for any peculiar or transient motion of the star using the following procedure. From the UCAC4 (Zacharias et al. 2012), PPMXL (Roeser et al. 2010), and Gaia DR3 (Gaia Collaboration 2016, 2021) databases, we collected a list of ten bright stars in the T CrA surroundings for which proper motion are available in all catalogs. These stars (listed in Table B.1) were selected on the basis of their having mag$_G$ ≤14 and lying within 10′ from T CrA. For these stars, we measured a long-term proper motion given by the difference in position between the UCAC4, PPMXL, and Gaia DR3 epochs. The long-term proper motion, defined as the motion of the star between different epochs of observations, is measured as:

$$\mu_\alpha \cos\delta = \frac{(RA_{Epoch1} - RA_{Epoch2}) * cos(DEC_{Epoch1})}{(Epoch1 - Epoch2)}, \quad \text{(B.1)}$$

$$\mu_\delta = \frac{(DEC_{Epoch1} - DEC_{Epoch2})}{(Epoch1 - Epoch2)}. \quad \text{(B.2)}$$

The analysis of the proper motion between the various epochs of the selected stars allows us to find a systematic offset between the average of the coordinate systems of UCAC4 and PPMXL with respect to Gaia DR3, which averages to 0.41±2.46 mas yr^{-1} in RA and 9.67 mas yr^{-1}±2.93 mas yr^{-1} in DEC for this specific region of the sky. For T CrA, we obtained an estimate of the proper motion of the star by correcting the long-term proper motion with the systematic offset, finding: $\mu_\alpha \cos\delta$ = 8.5 ± 2.5 mas yr^{-1} and μ_δ=-33.5±2.9 mas yr^{-1}. Considering the average proper motion of the on-cloud members, we find for T CrA: an apparent motion of $\mu_\alpha \cos\delta$ = 4.2 ± 2.5 mas yr^{-1} in RA and μ_δ=-6.2±2.9 mas yr^{-1} in DEC.

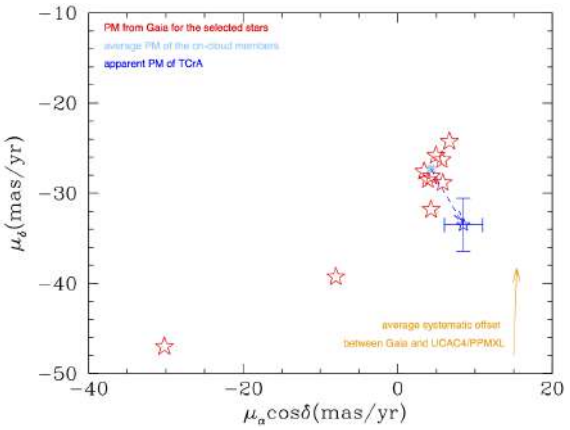

Fig. B.1: Proper motion of the ten stars reported in Table B.1. The cyan square represents the average proper motion for the on-cloud Coronet cluster obtained using Gaia DR2 data (Galli et al. 2020). The blue star is the calculated apparent proper motion of T CrA after correcting the long term proper motion for the systematic offset. In orange the direction of the systematic offset of the proper motion due to the different coordinate system.

Table B.1: List of the stars used to measure the proper motion offset.

	T CrA	V709 CrA	HD176269	HD176270	TY CrA	HD176423	V702 CrA	HD176386	HD176497	HD176018	CD-36 13202
(UCAC4)											
RA	285.494904	285.395229	285.263532	285.267908	285.420107	285.460076	285.508229	285.412217	285.528297	284.930902	284.920385
Dec	-36.963871	-37.015723	-37.060898	-37.061555	-36.876063	-36.664651	-37.128761	-36.890712	-36.361622	-36.788004	-36.588797
Ep. RA	1997.40	1985.45	1991.25	1991.25	1991.09	1990.50	1985.88	1991.25	1990.57	1988.91	1995.62
Ep. Dec	1997.77	1985.43	1991.25	1991.25	1990.52	1989.91	1984.44	1991.25	1990.28	1988.04	1995.74
(PPMXL)											
RA	285.494908	285.395224	285.263532	285.267908	285.420102	285.460076	285.508229	285.412219	285.528303	284.930902	284.920394
Dec	-36.963869	-37.015722	-37.060898	-37.061555	-36.876064	-36.664651	-37.128761	-36.890703	-36.361625	-36.788007	-36.588800
Ep. RA	1999.95	1988.00	1991.73	1991.18	1991.53	1991.41	1997.44	1991.14	1991.32	1991.23	1997.69
Ep. Dec	1999.95	1986.70	1991.64	1991.19	1991.76	1991.62	1998.14	1991.09	1991.38	1991.64	1998.44
(Gaia DR3)											
RA	285.494959	285.395278	285.263578	285.267966	285.420142	285.460103	285.508268	285.412238	285.528324	284.930856	284.920226
Dec	-36.963983	-37.015845	-37.061040	-37.061682	-36.876201	-36.664770	-37.128870	-36.890838	-36.361752	-36.788188	-36.589008
Ep. RA	2016.0	2016.0	2016.0	2016.0	2016.0	2016.0	2016.0	2016.0	2016.0	2016.0	2016.0
Ep. Dec	2016.0	2016.0	2016.0	2016.0	2016.0	2016.0	2016.0	2016.0	2016.0	2016.0	2016.0

Table C.1: Relative position of the secondary star (B) with respect to the primary star (A), and relative contrast (dH) in H-band of the secondary star with respect to the primary star, for a period of 29.6 years. The offset is defined in the direction of the semi-major axis of the stellar orbit.

Epoch	Offset B-A (mas)	dH (mag)
2007.54 (NACO)	-26.0±7.0	1.0±0.6
2016.25 (NACO)	-72.0±5.0	0.0±0.7
2016.60 (SPHERE)	-69.0±5.0	0.2±0.7
2018.36 (SPHERE)	-44.0±7.0	0.3±0.6
2021.50 (SPHERE)	11.0±7.0	1.0±0.5

Table C.2: Relative position of the secondary star (B) with respect to the primary star (A), and relative contrast (dH) in H-band of the secondary star with respect to the primary star, for a period of 59.2 years. The offset is defined in the direction of the semi-major axis of the stellar orbit.

Epoch	Offset B-A (mas)	dH (mag)
2007.54 (NACO)	91.0±7.0	1.0±0.2
2016.25 (NACO)	-39.0±8.0	0.0±0.3
2016.60 (SPHERE)	-44.0±8.0	0.0±0.2
2018.36 (SPHERE)	-70.0±7.0	0.0±0.2
2021.50 (SPHERE)	-108.0±6..0	0.0 ± 0.1

Appendix C: Binarity and light curve

The light curve of T CrA appears to be periodic. The period is found to be 29.6 years and it can be due to the presence of a binary star at the center of the T CrA system with a mass ratio of q~0.5±0.2 that is partially obscured by a disk seen edge-on and that has an offset with respect to the photocenter of the binary star of ~90 mas. The model of this binary system (described in Sect 3.1) is also able to account for the large-scale apparent proper motion measured in the period between 1998 and 2016. None of the images acquired in recent years with NACO (in 2007, 2016, and 2017) and SPHERE (in 2016, 2018, and 2021) show any clear evidence of a binary system for T CrA. Hence, we checked what the relative position of the secondary star with respect to the primary for every single epoch for which we have an image and the H-band contrast that should be observed. These quantities are shown in Table C.1. These values are all consistent with the fact that the binary system is not clearly resolved. Indeed, in the 2007, 2018, and 2021 epochs the separation between the two stars is too small to see the two sources separately. On the contrary, the two 2016 epochs have a larger separation, although they are still within $2\times\lambda/D$; this is so close that the secondary cannot be clearly separated from the primary. We notice, however, that in both images acquired around this epoch with NACO and SPHERE, the PSF appears elongated in the NW-SE direction, which corresponds to the direction of the major axis of the orbital motion of the binary system. The average position angle of the elongated PSFs acquired in 2016 is 130±15°, in very good agreement with the direction of the peculiar proper motion (PA_{PM}) measured and with the hypothesis that the orbit of the binary system is seen edge-on and perpendicular to the outflow. This elongation in different epochs supports then the scenario of a binary star. In a few years (i.e., in 2027), when the system is at its highest separation, the secondary component should be detectable with high-contrast images.

We have also considered the possibility that the period of the system might be double than the period measured in Sect. 2.3 (i.e., 59.2 years). While the light curve can be (in this case as well) easily reproduced, there are several observational shortcomings in this interpretation. First of all, we must notice that in this case the model predicts a mass ratio q as high as 0.9 and an offset of the disk of ~10 mas. This latter quantity is in disagreement with the observations, which instead show that the disk dark lane has an offset that is ten times larger. Moreover, the position of the center of the binary system as retrieved by assuming a 59.2 years period is not consistent with the motion of the system obtained from UCAC4/PPMXL and Gaia DR3 data. Additionally, in the SPHERE image acquired in 2021, the predicted separation between the primary and secondary component should be 108±6 mas, with a contrast of dH=0.5±0.1 mag, making it visible as a separate point source in the image. The relative position of the secondary star with respect to the primary for every single epoch for which we have an image, and the H-band contrast that should be observed are reported in Table C.2. The image does not reveal the presence of the secondary star. Given these shortcomings between observations and the output of the model, we exclude that the period of the binary star is 59.2 years. Figure C.1 and C.2 show the corner plot of the derived quantities of the model used in Sect. 4.1 to model the light curve assuming a period of 29.6 years or the double (59.2 years). The light curve for the period of 59.2 years is shown in Fig. C.3.

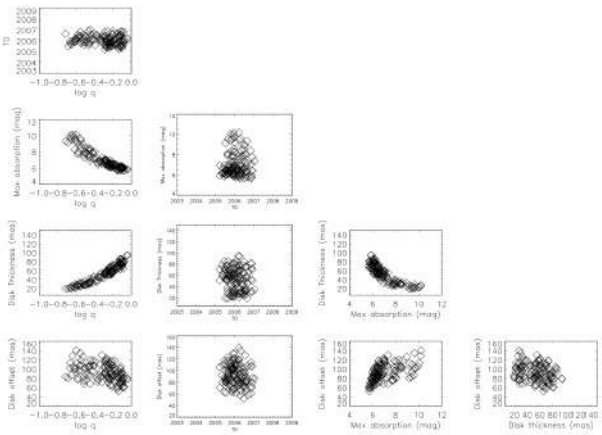

Fig. C.1: Corner plot showing the results of the MC parameters estimation for the model described in the paper when a period of 29.2 years is considered. The plots show the 2D joints posterior densities of all couple of parameters.

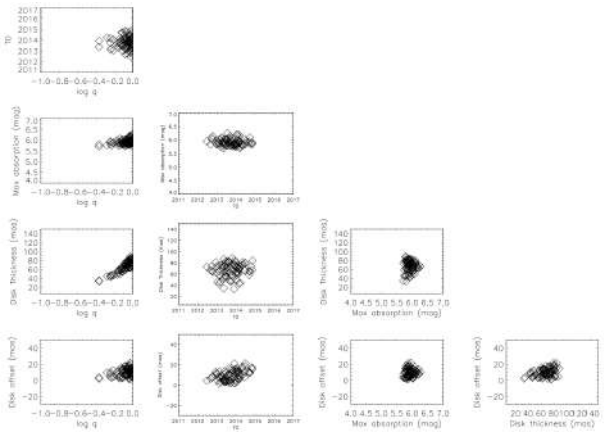

Fig. C.2: Corner plot showing the results of the MC parameters estimation for the model described in the paper when a period of 59.6 years is considered. The plots show the 2D joints posterior densities of all couple of parameters.

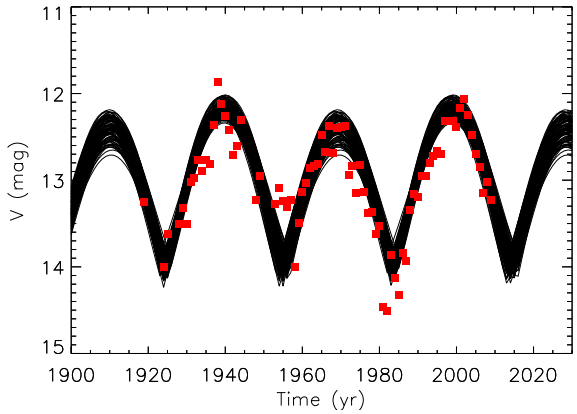

Fig. C.3: Light curve of T CrA (red points) compared to the light curves computed with the MC model (black lines) assuming a period of 59.2 years.